Enhanced Ground Penetrating Radar Analysis for Buried Pipeline Characterisation and Leakage Detection

Shokri, N. H.,[1] Darwin, N.[2*] and Amin, Z. M.[3]
[1]Department of Geoinformation, Faculty of Built Environment and Surveying, Johor Bahru, Johor, Malaysia E-mail: hazimahshokri@gmail.com
[2]Geospatial Imaging and Information Research Group (Gi2RG), Department of Geoinformation, Faculty of Built Environment and Surveying, Johor Bahru, Johor, Malaysia, E-mail: norhadija2@utm.my*
[3]Geomatic Innovation Research Group (GnG), Department of Geoinformation, Faculty of Built Environment and Surveying, Johor Bahru, Johor, Malaysia, E-mail: zulkarnaini@utm.my
Corresponding Author

DOI: https://doi.org/10.52939/ijg.v22i1.4715

Abstract
This study presents an advanced approach to Ground Penetrating Radar (GPR) for characterising buried pipelines and detecting water leakages. GPR is a non-destructive technique used to detect subsurface dielectric objects such as pipelines. The research combines theoretical modelling, experimental validation, and numerical simulation across various pipe materials (metal, fiberglass, PVC) and soil types (clay, sand, and silt). Hyperbolic signatures and power reflectivity in radargrams were analysed to estimate pipe radius, with an accuracy of 75.7%. Methods for feature recognition, anomaly detection, and signal enhancement were applied to improve the identification of buried utilities and leak zones. The study incorporates four comparative approaches: attenuation characteristic analysis, time-frequency spectral analysis, and Finite-Difference Time-Domain (FDTD) simulation. Corroded pipes are effectively detected through attenuation analysis, while cracked pipes are identified using time-frequency spectral methods. FDTD simulations reveal that sand-based models are computationally less intensive than those involving finer soils like clay or silt. Signal filtering techniques, including fitted velocity modelling and hyperbola extraction, improve the clarity and reliability of radargrams. In conclusion, this integrated GPR-based approach significantly advances underground pipeline diagnostics, offering a powerful tool for infrastructure maintenance, leak detection, and utility mapping in urban environments.

Keywords: Advanced Filtering, GPR, Leakage Detection, Pipeline

1. Introduction

Ground Penetrating Radar (GPR) has emerged as one of the most reliable and effective non-destructive technologies for subsurface exploration and infrastructure assessment. Widely applied across fields such as civil engineering, environmental studies, and geophysics, GPR provides detailed insights into the location, size, condition, and structural integrity of buried objects like pipes, cables, and voids [1]. This technology operates by transmitting high-frequency electromagnetic waves into the ground and recording the reflected signals from subsurface features. These reflections, displayed in radargrams, often appear as hyperbolic patterns, which can be analysed to determine the characteristics of underground objects [2].

GPR is particularly advantageous in assessing cylindrical utilities such as water pipelines and sewerage systems. Its non-invasive methodology not only preserves the ground surface but also allows for efficient and repeatable investigations [3]. However, challenges arise in accurately interpreting radargrams due to soil moisture, material composition, and signal attenuation. Soil conditions, including dielectric permittivity and conductivity, significantly affect signal propagation and reflection [4] and [5]. Furthermore, pipe material variations from metallic to non-metallic types such as PVC, fiberglass, or HDPE influence signal detectability and strength [6] and [7]. This study seeks to improve the accuracy of subsurface pipe profiling and leakage detection using GPR. One focus is determining the geometric properties of buried pipelines, specifically pipe radius, through hyperbolic signatures and power reflectivity analysis [8] and [9]. Another dimension of the study incorporates advanced signal processing techniques, such as spectral analysis, Finite-

Difference Time-Domain (FDTD) simulations, and 3D visualization, to enhance water leakage detection and understand the interaction between electromagnetic signals and subsurface conditions [10] and [11]. By combining theoretical modelling, synthetic simulations, and field experiments, this study aims to develop a robust approach for identifying underground utilities and their anomalies, providing substantial benefits for urban infrastructure maintenance and planning [12] and [13].

1.1 Hyperbolic Signatures of the GPR

GPR radargrams undergo a number of digital image processing steps as GPR antenna travels along the surface, followed by variable power reflectivity within the energy zone. The power reflectivity for vertically oriented migration traces is created, and while calculating the radius of the pipes, the distance between variant power reflectivity and the long dimension radius of an energy footprint is considered [8]. Antenna-produced electromagnetic waves generally transmit radar energy as an elliptical cone onto the surface. The elliptical cone transmission is typically stretched parallel to the scanning direction at different depths, establishing the cone form and energy radius (E/2). Energy radius can be determined using Equation 1:

$$0.5E = 0.25\lambda + \frac{H}{\sqrt{\varepsilon r + 1}}$$

Equation 1

Where:

E is the long dimension radius of the energy footprint,
λ is the centre frequency wavelength of the radar energy,
H is the depth from the concrete surface to reflection surface,
εr is the average relative dielectric permittivity of the material from the surface to depth (H).

The power reflectivity of GPR radargrams is calculated by varying the coefficients of reflection from the beginning to final reflection signal within the energy zone as the antenna moves over the surface. The model's schematic is shown in Figure 1. Variations cause the created variation power reflection, and the generated variant power reflectivity is caused by a circumferential cylindrical object (pipe). It can be proved by Equation 2:

$$Scor = L - E$$

Equation 2

Where:

$Scor$ is the corresponding circumference length of the pipe,
L is length of the signal change of power reflectivity,
E is the long dimension radius of the energy footprint at depth H.

The radius of the pipe is calculated by the following Equation 3:

$$r = \frac{Scor}{2\pi} = \frac{L - E}{2\pi}$$

Equation 3

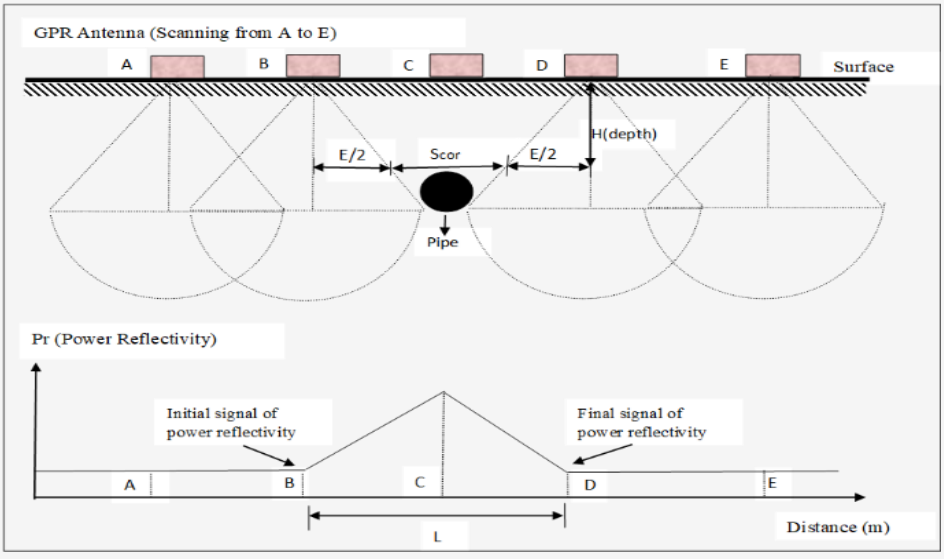

Figure 1: The effect of the power reflectivity (Pr) of the buried pipe

The approaches to interpreting the radius of the pipes buried have been determined. GPR has the benefit of high resolution and the ability to detect magnetic and non-magnetic objects using surrounding signals. The technique was applied to various types of pipelines, such as fiberglass, PVC, and metal pipes.

1.2 Depth Penetration

The depth of the GPR survey depends on the transmitting frequency, the transmitted power, and the conductivity of the ground or medium investigated, depth range varies from 25 mm to 40 m, but is typically 0.1–5 m for most geotechnical applications [14]. Deeper penetration is possible with lower frequencies (e.g. 25–100 MHz) provide the long wavelength compare to high frequencies, providing that the ground is not too conductive. The electrical conductivity of the sediments is the main factor influencing how quickly the GPR signal attenuates. The penetration depth will drop dramatically if the sediment has a high electrical conductivity. Adequate signal penetration may be challenging below the groundwater table. Obtaining relevant findings below the antenna's 1-2 wavelengths is nearly difficult in highly conductive zones like saturated clays or saline marshes. When operating in optimal conditions, GPR systems operating at frequencies lower than 100 MHz can be achieve penetration depths exceeding 10 meters. At 25–50 MHz, penetration distances of more than 100 meters are achievable in dry crystalline rock, such as granites. The majority of GPR surveys in the field of civil engineering are carried out at frequencies ranging from 1.5 GHz to 400 MHz, with a typical penetration depth of 0.3–3m. It is mostly utilized in concrete constructions and utility mapping.

1.3 Numerical Modelling

Numerical modelling enhances the precision of GPR radargram interpretation by addressing complex lining flaws. It helps determine the spatial position, distribution, and physical qualities of subsurface objects. Interpretation relies on analysing the signal waveform, amplitude, phase, and frequency spectrum of echoes. The study employs enhanced simulation methods such as FDTD, signal analysis, and defect mapping to evaluate GPR radargrams. These simulations produce matrices for the relative dielectric constant, magnetic permeability, and quality factor structures. The synthetic model in the radargram is constructed based on these matrices, ensuring no attenuation, absorption, or distortion of the hyperbola form [11]. In summary, the research leverages advanced GPR technology and numerical modelling to accurately assess the condition of underground water pipelines. By using commercial programs and sophisticated simulation methods, it aims to improve the reliability and efficiency of utility infrastructure maintenance [1].

1.4 Leak Mapping and GPR for Monitoring Corrosion

Leak mapping is a crucial process in the maintenance of water distribution systems. It allows for the visualisation of the entire history of leaks within the system. GPR plays a significant role in this process by identifying cracks and corrosion in pipes buried underground [12]. GPR is used to monitor the corrosion of reinforcement in buildings. This is done by examining the reflection amplitude of reinforcing bars, which changes as corrosion progresses. Corrosion, particularly in metal structures, is a major issue often exacerbated by the presence of chloride-contaminated sediment [12]. The presence of chlorides significantly accelerates the deterioration of metal structures. Environmental factors, such as temperature and humidity, also impact the rate of corrosion in metal pipes. High moisture levels and the presence of chlorides are especially influential, as they are detectable and influence GPR signal [15]. When the chloride content in the metal reaches a certain threshold, it can disrupt the alkaline environment that normally protects the metal. If sufficient oxygen and moisture are present, the metal will begin to corrode.

The dielectric permittivity of the medium, which represents its ability to store electromagnetic wave energy, affects the velocity of the waves transmitted through it [16]. Dispersion, a phenomenon in which different frequencies of the wave propagate at different speeds, which can distort the wave phase. In environments with moisture, higher frequency components of the GPR signal respond more quickly than lower frequency components. This results in decreased signal amplitude, as moisture acts as a low-pass filter, attenuating higher frequencies [5]. As the chloride concentration increases, signal attenuation also increases. As corrosion progresses and accumulates, the signal energy captured by GPR increases. Active corrosion develops unevenly, with higher corrosion risks indicated by more negative values in the GPR signal, which increases the energy intensity. This leads to a more complex interface, involving concrete, rust, air, and steel, which causes stronger reflections of the GPR signal from corroded rebars. The accumulation of corrosion results in a stronger GPR signal [17]. A new method for regular monitoring of reinforcement corrosion in concrete has been developed using high-frequency GPR systems [18]. This method allows for the visualization of the cumulative development of corrosion. Interestingly, in areas where severe steel

section loss has occurred due to pitting corrosion, the amplitude of the GPR-reflected wave from the reinforcement is unexpectedly small. The amplitude of the reflected wave is more sensitive to corrosion than the central frequency. As corrosion advances, the amplitude of the reflected wave increases, and the travel time of the signal decreases, indicating the progression of corrosion. In summary, GPR is an invaluable tool for detecting and monitoring the condition of underground water pipes and metal structures. By analysing the reflection amplitudes and other characteristics of GPR signals, it is possible to identify cracks, corrosion, and other forms of deterioration. Environmental factors such as moisture and chloride content significantly influence the GPR signals, making it possible to assess the extent of corrosion and plan appropriate maintenance measures.

2. Materials and Methods

This study employed a comprehensive methodology integrating theoretical modelling, physical experiments, and advanced data processing to evaluate the performance of Ground-Penetrating Radar (GPR) in detecting and characterising buried pipelines, as well as identifying leakage. GPR works by transmitting high-frequency electromagnetic waves into the ground. When these waves encounter subsurface materials with different dielectric properties, part of the signal is reflected back to the surface and captured by a receiving antenna. These reflections are compiled into a radargram a visual profile showing subsurface features based on signal strength and travel time. Cylindrical objects, such as pipelines, produce distinct hyperbolic patterns in radargrams. The study used the mathematical model by [8], which incorporates relative dielectric permittivity, to estimate pipe size and location from these hyperbolic signatures.

The methodology was divided into three modules. The first involved creating synthetic models using MATGPR software to simulate hyperbolic patterns produced by buried pipes of different materials and in various soil conditions. These synthetic radargrams served as benchmarks for comparison with experimental data. The second module consisted of physical experiments using a custom-built testbed containing different pipe materials such as HDPE, UPVC, MSCL, and mild steel, buried in sand, clay, and silt. Leak conditions were simulated by introducing cracks and corrosion in the pipes. The third module focused on data collection and processing. Radargrams from both simulations and experiments were processed using standard and advanced filtering techniques, including background removal, gain adjustments, and noise reduction, to enhance signal clarity and feature recognition. In total, five pipes were used: two fiberglass pipes (16.7 cm and 6.2 cm in diameter), two PVC pipes (11.6 cm and 4.0 cm), and one metal pipe (3.0 cm), each approximately 1 meter in length. This integrated approach allowed for the accurate analysis of how different soil types and pipe materials affect GPR signal behaviour, ultimately supporting more reliable detection, condition assessment, and maintenance of underground pipeline infrastructure. Figure 2 shows the length and diameter of the fiberglass pipes, PVC pipe diameters, and metal pipe.

Figure 2: The length and diameter of the fiberglass pipes, PVC pipe diameters, and metal pipe

3. Result and Discussion

The signal's amplitude in the wiggle box determines the reflectivity power. The reflectivity power values were taken at the beginning, center, and end of the hyperbola curve. Table 1 shows the power reflectivity values for all sizes and types of buried pipes.

Table 1: The power reflectivity values for every type and size of buried pipes hyperbola form's starting point, its centre, and its end

	Power Reflectivity (MHz)		
Types of Pipes/ diameter (cm)	**Beginning hyperbola**	**Centre hyperbola**	**Ending hyperbola**
Metal (3.0)	45.900	1151.5	283.611
Fiberglass (16.7)	124.370	-81.351	96.221
Fiberglass (6.2)	169.744	-1084.8	118.891
PVC (11.6)	82.741	1191.6	-1.23027
PVC (4.0)	-31.047	-2572.8	31.456

Table 2: Comparison between GPR estimation of pipes radius and actual pipes radius buried in clay test bed

Types	Energy Footprint, E (m)	Variation Distance, L (m)	Estimation Radius, R (m)	Actual Radius of Pipes (m)	Error (%)
Metal	0.309	0.203	0.017	0.015	12.3
Fiberglass	0.437	0.858	0.067	0.084	19.7
Fiberglass	0.193	0.378	0.029	0.031	5.0
PVC	0.359	0.840	0.077	0.058	32.1
PVC	0.271	0.429	0.025	0.030	16.2

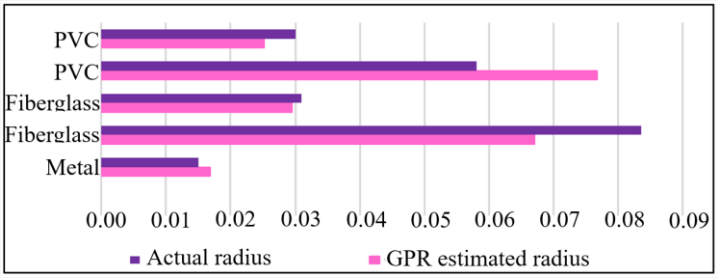

Figure 3: A bar chart to visualize the radius differences between actual and GPR estimation

The effects of electromagnetic waves through various types and sizes of buried pipes have been measured, refer Table 1. Smaller buried pipes have a higher power reflectivity on the centre hyperbola than bigger pipes. According to pipes type, although it reflects both positive and negative signals, the reflections are equally important. Fiberglass pipes show more reflection in this experiment because of their larger size and higher dielectric permittivity. In contrast, metal pipes are more conductive to electromagnetic waves despite having a lower power of reflection due to its smaller size. The table clearly shows that the power reflectivity at the beginning and end of the hyperbola for each pipe buried are varies. This might be explained by the unsymmetric pinpoint on the beginning and ending of the hyperbola formation, plus the test beds not being as compact as it could be, which would cause variances in air porosity beneath. Table 2 presents a comparison of the GPR estimate of the buried pipe's radius, computed by the aforementioned data processing approach, and the actual pipe radius. Meanwhile, Figure 3 shows the bar chart of radius differences between actual and GPR estimation.

Based on Table 2. the metal pipe's deviation from the true radius is only +0.0018m. On the other hand, the fiberglass pipes with a radius of 0.0835m consume a different of -0.0164m, whereas the difference for the fiberglass pipes with a radius of 0.0310m is just -0.0016m. Additionally, PVC pipe with radius of 0.0580m consume a different of +0.0186m, while the difference between the 0.0300m radius PVC pipe is -0.0049m which is smaller than actual radius.

3.1 Filtering Process

There are two different types of filtering processes. The first is normal filtering using typical GPR software; in this study, Reflex 2D Quick software was used. The second aspect of filtering is advanced filtering, which is performed using MATLAB software and a MatGPR function. All of the data underwent the normal filtering procedures after data collection. In all GPR data, including in the utility practice, the procedure is routinely employed and is a fundamental data procedure. The filtering process includes gain function, background removal, subtract DC shift, subtract mean (dewow), and static correction. All GPR software data processing programmes contain these functions, including Reflex W, GPRMax, Impulse Radar, Mala, RGPR, and many others.

In experiment case 1, there are three sets of data: before, during, and after water induced instead of sand and clay sediment test bed. The radargram produced by the Reflex 2D Quick programme shows the hyperbola curves quite vividly. As a result, the fitted velocities for each hyperbola are also presented. Figure 4 show the radargram of sand sediment test bed. A wiggle radargram is shown to help viewers comprehend the hyperbola more clearly. The wiggle signal gives central contrast of signal amplitude of the strong reflectivity signals. The Reflex 2D Quick program's radargram clearly depicts the hyperbola curves. As a result, each hyperbola's fitted velocities in sand and clay sediment are collected and presented in Table 3.

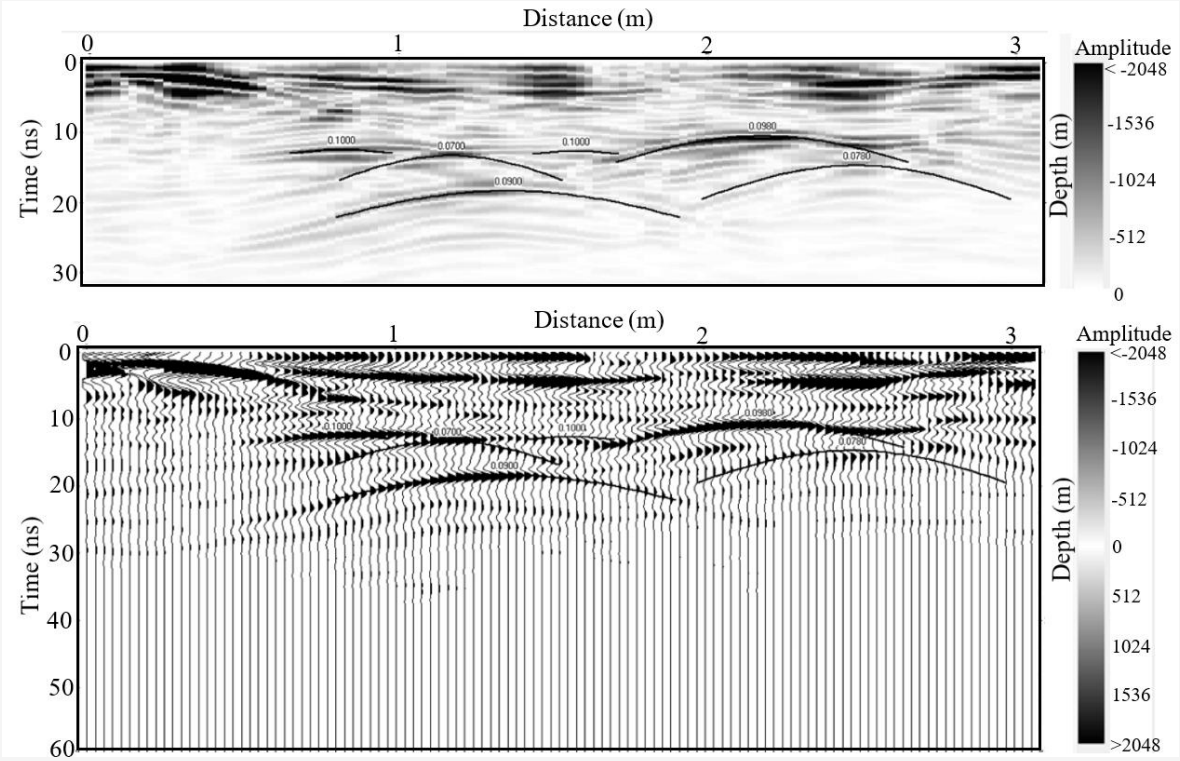

Figure 4: Sand sediment test bed before water induced fitted velocity with wiggle radargram

Table 3: The fitted velocity in sand and clay test bed

Pipes	Condition	Fitted Velocity (nm/s)					
		Sand			Clay		
		Before	During	After	Before	During	After
HDPE	Healthy	0.100	0.070	0.095	0.080	0.100	0.085
UPVC		0.070	0.085	0.095	0.080	0.090	0.080
MSCL		0.090	0.110	0.090	0.060	0.060	0.060
HDPE	Unhealthy	0.100	0.090	0.090	0.060	0.090	0.090
UPVC		0.980	0.100	0.090	0.075	0.080	0.070
MSCL		0.078	0.100	0.095	0.075	0.075	0.065

The data from the tables indicate that the highest velocities recorded are typically observed when water is injected into the soil. This is further supported by the radargram, which visually represents radar data. As soil moisture increases, the radargram shows a flattening of the hyperbolic shapes typically seen in radar reflections. These hyperbolas are indicative of the radar signal's travel path and reflection points. This implies that the high level of soil moisture, increases the signal's resistance, allowing for a higher velocity of the radar waves and subsequently longer travel times. Therefore, the correlation between increased soil moisture and augmented radar signal velocity is clearly demonstrated through the radargram's visual evidence and the tabulated velocity data. This means the radargram provides verification of the water leaks signal reflectivity. Next, in experiment case 2, there are three sets of data: 1 year (new), 10 years (mild), and 34 years (old) mild steel pipes buried in silts sediment. Figure 5 shows the three radargrams of the test site area. Based on the radargram above, the mild steel pipes are visible. However, the radargram of the 10-year old mild steel pipes is quite strained due to the damp subsurface, and the hyperbola of the pipes can be seen in multiple reflections. The generated radargram shows the hyperbolic curves quite indistinctly with increasing age. The fitted velocities for each hyperbola can be found in Table 4.

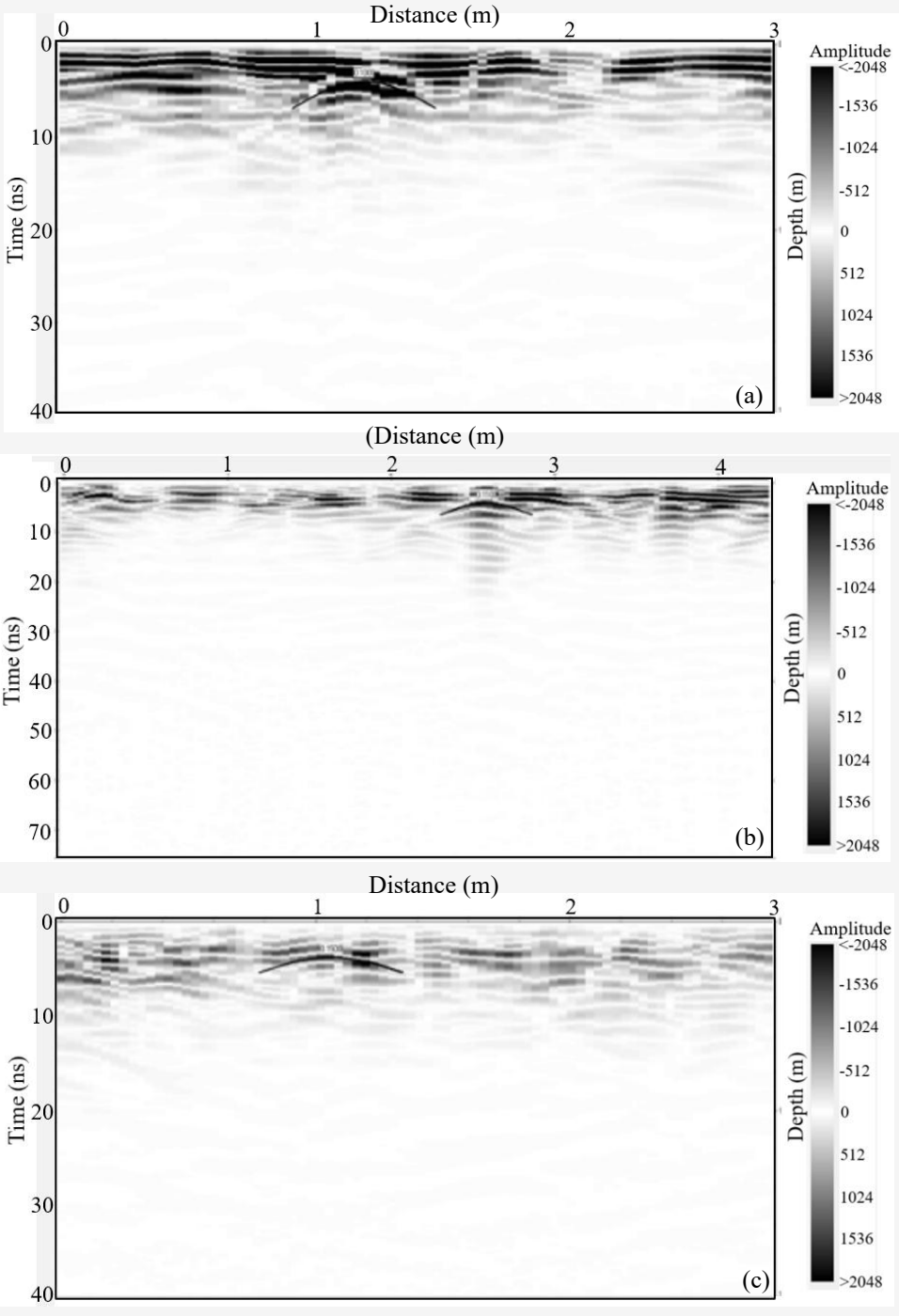

Figure 5: Radargram of experiment case 2, on mild steel (a) 1 year (b) 10 years, and (c) 34 years

Table 4: The mild steel pipes fitted velocity in silts sediment

Mild steel pipes (year)	Fitted Velocity (nm/S)
1	0.100
10	0.110
34	0.150

Table 4 shows that the highest installation speed is typically observed at the location of the oldest mild steel pipe. The radargram further illustrates that higher soil moisture levels cause the characteristic hyperbolic shapes of the radar reflections to flatten. This flattening effect suggests that the radar signal travels faster through the soil, covering greater distances in higher amounts of time. Increased soil moisture appears to increase resistance to the radar waves as well, thereby increasing both the velocity and the travel time of the signal. Thus, the correlation between soil moisture, signal velocity, and travel time is evident from both the radargram and the data in Table 4.

3.2 Advanced Filtering Radargram

There are different types of advanced filtering described in the MatGPR Release 3 Manual and Technical Reference. However, according to the study, only two types of advanced filtering systems are applicable and beneficial for water leaks. The filters are the global background removal filter and the directional wavelet filter. Global background removal meant removing the data's "global" background traces. The average trace is calculated by adding up all the traces and dividing by the total number of traces. The stacking procedure reduces signal volatility and enhances signal coherence (or anomalies), making the hyperbola in the radargram more vivid. The strong noise was completely removed with the help of the filter.

Alternatively, directional wavelet filters can improve signals and retrieve information based on scale-selective 1D wavelet filters and orientation and scale selective 2D wavelets. The filter also combines the Gabor filters in its function. In terms of texture analysis, a Gabor filter, which bears the name of Dennis Gabor, is a linear filter that determines whether a certain frequency content is present in the radargram in certain directions in a limited area around the examined point or area. Due to the presence of an air gap below the surface, the hyperbolic anomaly of the radargram appears to be weak. To determine which filter is best suited for this study, the signal attenuation characteristic was applied to both filters. However, the radargram must first be converted to Radan 16-bit. Reflex 2D Quick software is used to convert the radargram. The raw data attenuation characteristic, the global background removal, and the directional wavelet filter attenuation characteristics are shown in Figure 6.

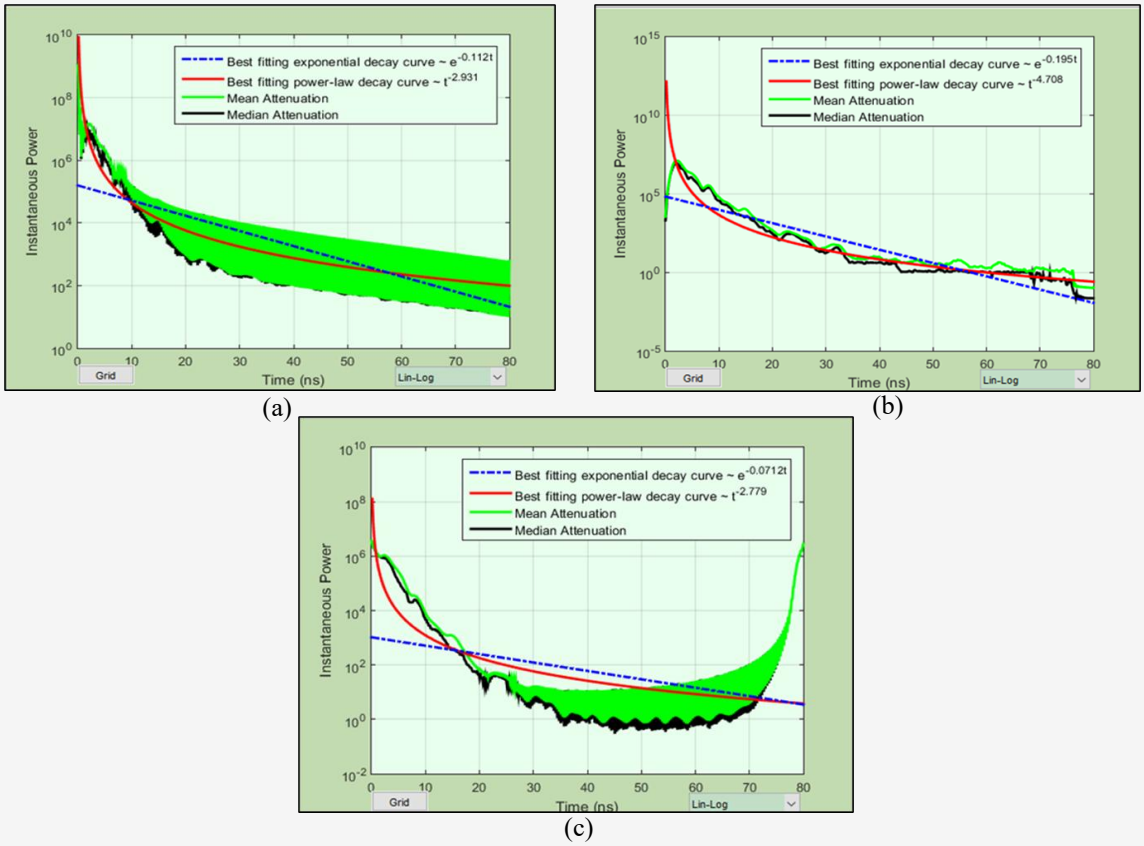

Figure 6: The attenuations characteristic of the: (a) raw data, (b) global background removal filter and (c) directional wavelet filter

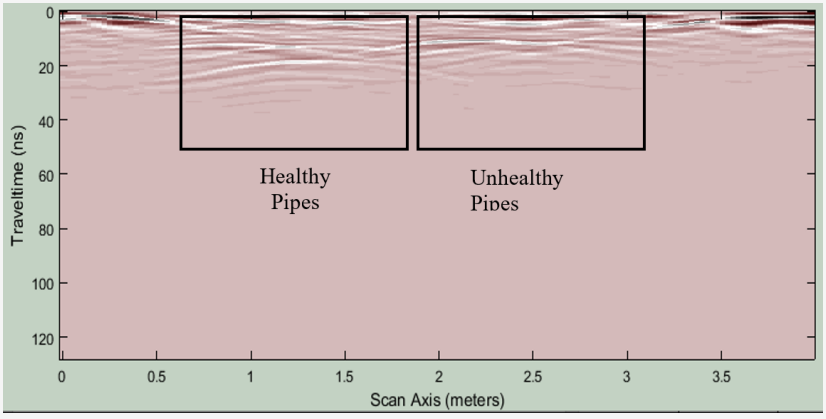

Figure 7: Processed GPR radargram before water induced

The best-fit advanced filtering was selected based on the abovementioned figures. While the directional wavelet filter only considers the initial attenuation of the radargram and encapsulates higher attenuations at the end of the radargrams, the global background removal demonstrated to reduce virtually all attenuations from the raw data. Therefore, a global background removal filter was applied to all associated radargrams in this study. Figure 7 shows the processed GPR radargram of experiment case 1. The figures show an example of the observed data prior to water injection into a sand-sediment test bed.

The hyperbola observed before water induction was more pronounced compared to the hyperbola observed during and after water induction. This indicates that hyperbolas form more distinctly in dry conditions and tend to flatten in wet conditions. The same procedures were applied to the clay sediment test bed. Based on the radargrams processed by advanced filtering in experiment case 1, it is apparent that the dry and wet phases of hyperbola formation can be clearly distinguished. The discrepancy between healthy and unhealthy pipes is more apparent than in the radargrams processed with normal filtering. As soil moisture increases, the hyperbola in the data processed with advanced filtering becomes blurrier, flatter, and thicker. Experiment case 2 was then subjected to global filtering to remove the background. The processed GPR radargram from Experiment Case 2 is shown in Figure 8. The figures depict the observed data of mild steel water pipelines aged one year, ten years, and 34 years in silts sediment.

According to Figure 8, the hyperbola formation for mild steel pipelines fades with age. The fading hyperbola indicates a decrease in signal reflection. Although the 34-year-old mild steel water pipes have the lowest signal reflection, they appear to be in good condition as they are not connected to interferers. Meanwhile, the 10-year-old mild steel water pipelines seem to be interfering with other substances, such as water, leading to redundant signal reflectivity in the radargram.

3.3 Comparative Approach Function

Power law and exponential decay are both included in the fitting model. Table 5 lists the best-fitting exponential decay for experiment case 2. The exponential decay is a "best fit" since it goes over most plotted points and appears to follow the data's growth rate. Power decay occurs in only a few places and does not appear to follow the degree of growth or exponential decay. The key distinction is that exponential decay and power law decay grow as metal oxidation and corrosion increase. Figure 9 shows the attenuation characteristic graph for 1, 10, and 34-year old pipe radargrams.

One of the main components in determining how corroded and cracked a buried pipe is the electromagnetic signal's attenuation. The unstable dielectric constant between the pipe and its corrosions leads to a bigger signal attenuation. The instantaneous power in experiment case 2 decreases as the pipeline ages. The graph of the experiment case 2 attenuation characteristic shows that as mild steel pipes aged, the instantaneous power on the y-axis slightly decreased. This demonstrated that signal reflection has decreased, and signal attenuation has increased. However, the 10-year-old mild steel pipe radargram has a significant water content, which affects the stability of the corresponding analysis and results in a greater mean attenuation. As a result, water leakage from corroded pipes can also be detected by the attenuation characteristics.

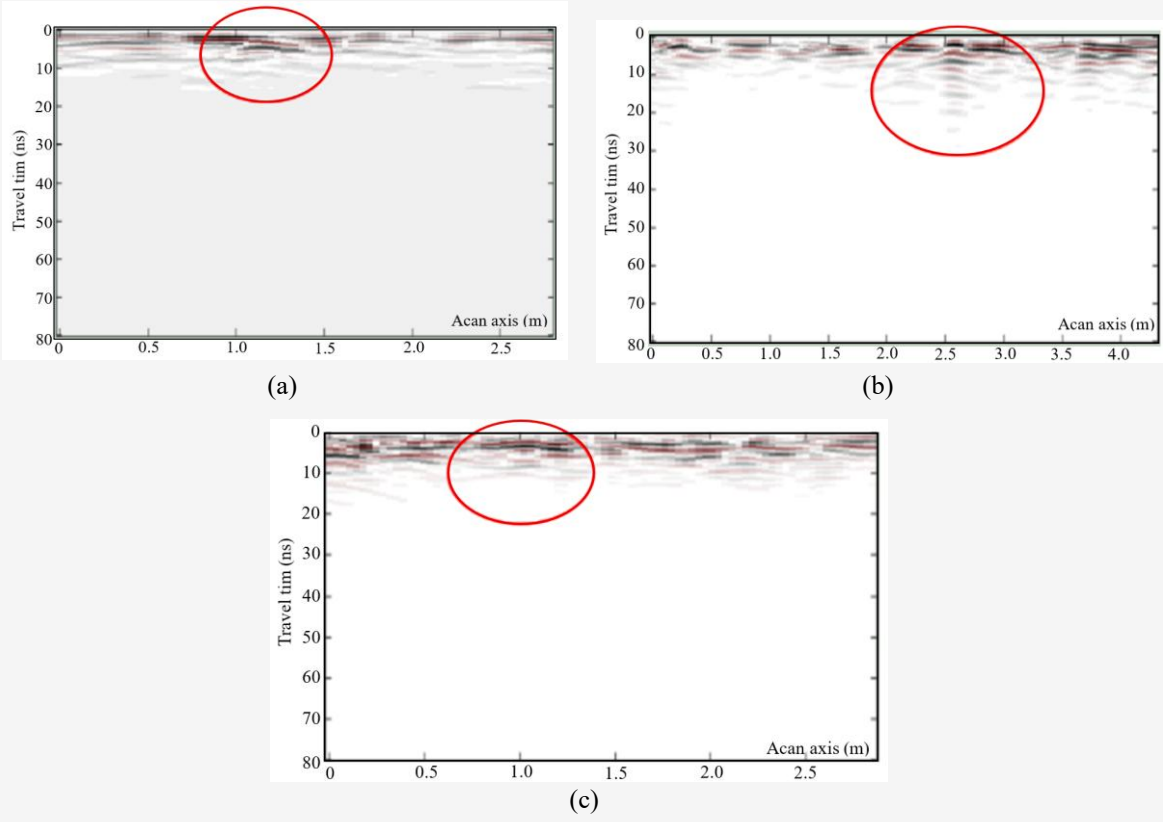

Figure 8: Radargram of mild steel water pipeline based on ageing (a) 1 year, (b) 10 years and (c) 34 years

Table 5: Experiment case 2 attenuation characteristic

Sediment	Duration (Years)	Best Fitting exponential decay curve~e (t)	Best Fitting power law decay curve (t)
Silts	1	-0.112	-2.931
	10	-0.108	-2.822
	34	-0.102	-2.659

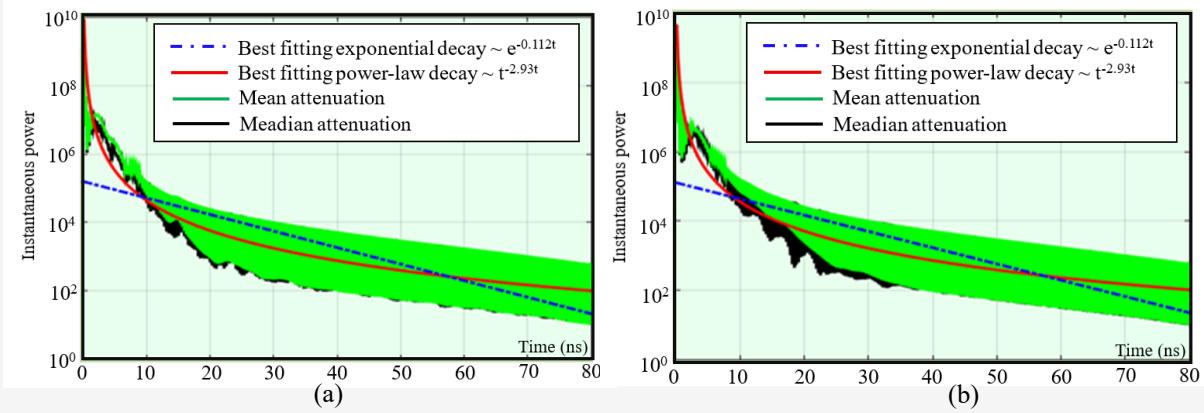

Figure 9: The attenuation characteristic graph for pipe radargram:
(a) 1 year, (b) 10 years, and (c) 34 years (continue next page)

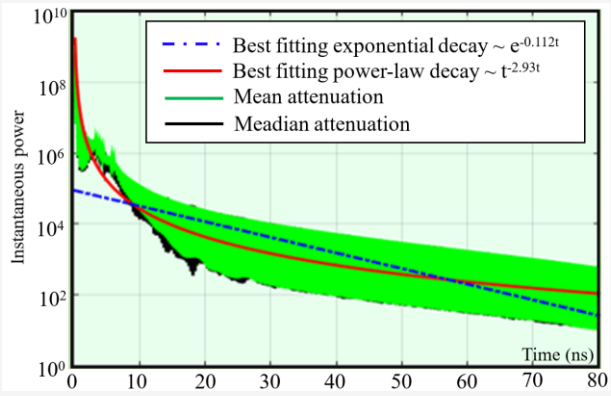

(c)

Figure 9: The attenuation characteristic graph for pipe radargram:
(a) 1 year, (b) 10 years, and (c) 34 years (continue from previous page)

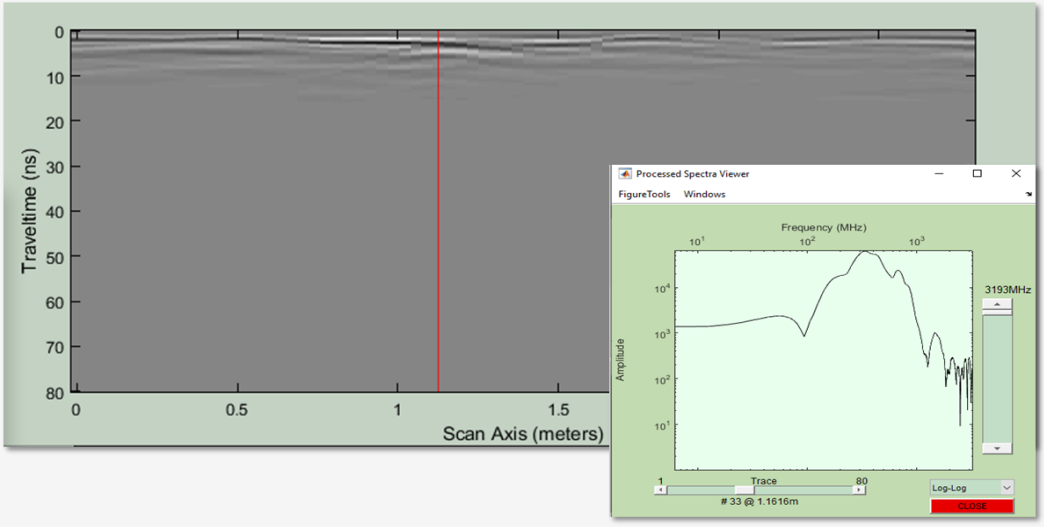

Figure 10: The abnormal amplitude obtained thru inspection trace from the red line marking

3.4 Time Frequency Spectra Analysis

There is a feature that tolerates tracking each radargram anomaly individually. The abnormal amplitude can be tracked and examined using impact trace spectra and a time-frequency content viewer. This function was used to detect water leaking as the abnormal amplitude is typically higher than its surroundings. Figure 10 shows the processed radargram being inspected. Furthermore, a time-frequency content viewer is a suitable function that can be used to identify water leakage. The time-frequency content viewer function allows visualising the flow of the water leakage. The abnormal amplitude colour difference makes the interpretation much easier. Figure 11 and Figure 12 shows the time-frequency content viewer of experiment case 1. The time-frequency viewer was used to inspect traces of unhealthy lines. As shown above, the movement of water content in the sand sediment test bed after water induction is faster than in the clay sediment test bed. Sand sediment operates at a frequency range of approximately 0.2 GHz to 0.3 GHz, while clay sediment operates at a range of approximately 0.2 GHz to 0.4 GHz. In this function, water leakages time frequency tends to exhibit a more blurring effect, and the signal reflection appears to fade away. Generally, modulation and multiplexing are more efficient when using the time-frequency distribution. Utilizing these functions from the MatGPR software aids in comprehending the collected data. Furthermore, the time-frequency content viewer feature helps in locating water leakages and analysing the flow.

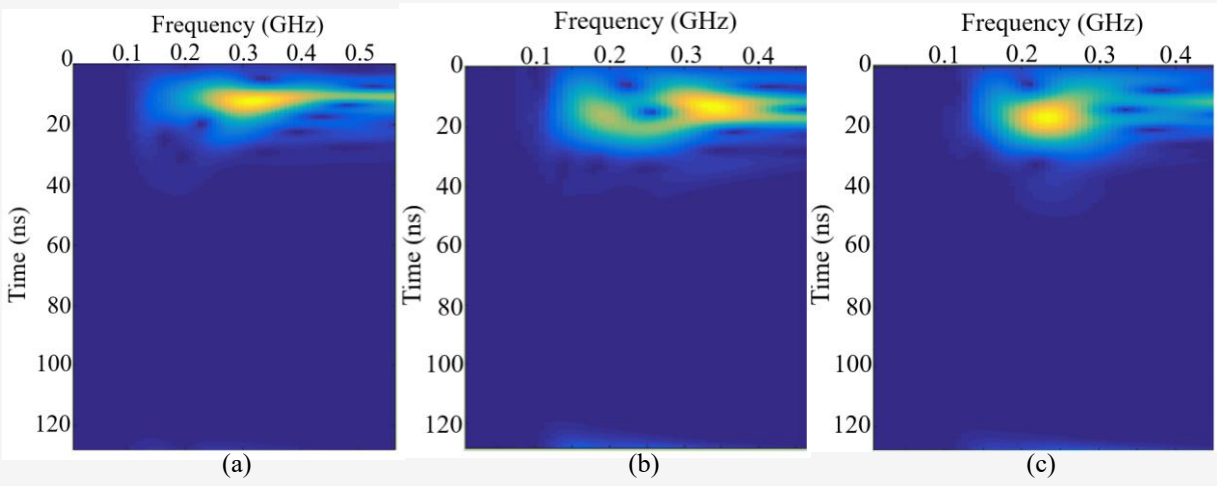

Figure 11: The time frequency content viewer of sand sediment test bed:
(a) before water induced, (b) during water induced, and (c) after water induced

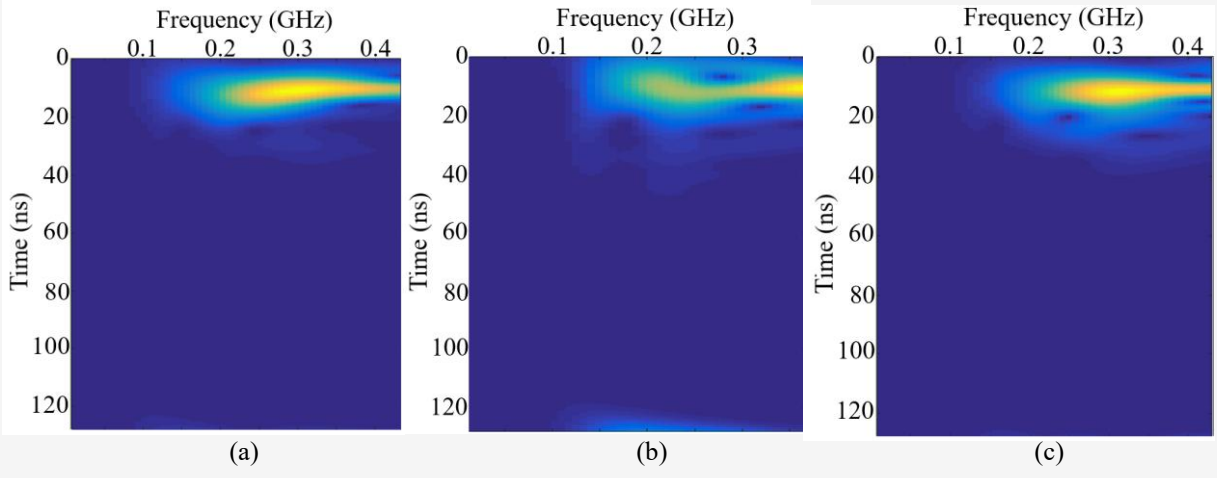

Figure 12: The time frequency content viewer of clay sediment test bed:
(a) before water induced, (b) during water induced, and (c) after water induced

4. Conclusion

This study demonstrates that advanced Ground Penetrating Radar (GPR) techniques significantly enhance the accuracy and efficiency of buried pipeline characterisation and water leakage detection. Combining theoretical modelling, physical experimentation, and advanced signal processing techniques including conventional filtering methods the study provides a comprehensive framework for subsurface utility analysis. Distinct hyperbolic patterns generated by different pipe materials and sizes were successfully identified and used to estimate pipe radius, achieving a model accuracy of 75.7%. Applying GPR across various soil types, including sand, clay, and silt, further confirmed that soil conductivity and moisture content directly influence signal clarity, attenuation, and velocity.

The study also highlights the role of comparative techniques such as attenuation characteristic analysis, time-frequency spectral analysis and Finite-Difference Time-Domain (FDTD) modelling enhancing detection sensitivity. These approaches allowed for the differentiation between cracked and corroded pipes and revealed that moisture-induced signal distortion can be minimised with appropriate filtering techniques. The findings show that this integrated GPR approach is a powerful and practical diagnostic tool for infrastructure maintenance and leak detection. It offers significant advantages in cost-effectiveness, non-invasiveness, and real-time data interpretation, making it highly suitable for smart utility mapping and sustainable urban infrastructure management.

Acknowledgement
The authors express their gratitude to the Ministry of Higher Education (funded under research votes 5F634) and Universiti Teknologi Malaysia for their kind support and GUP Tier 1 (funded under research votes 19H90) The authors also fully acknowledged Mr. Akmal from Syarikat Air Johor (SAJ) for support, which makes this important research viable and effective.

References

[1] Latif, J., Shakir, M. Z., Edwards, N., Jaszczykowski, M., Ramzan, N. and Edwards, V., (2022). Review on Condition Monitoring Techniques for Water Pipelines. *Measurement,* Vol. 193. https://doi.org/10.1016/j.measurement.2022.110895.

[2] Iftimie, N., Savin, A., Steigmann, R. and Dobrescu, G., (2021). Underground Pipeline Identification into a Non-Destructive Case Study Based on Ground-Penetrating Radar Imaging. *Remote Sensing,* Vol. 13(17). https://doi.org/10.3390/rs13173494.

[3] Pang, J. C., Suzuki, M. and Kato, Y., (2023). Iterative Application of Generative Adversarial Networks for Improved Buried Pipe Detection from Images Obtained by Ground-Penetrating Radar. *Computer-Aided Civil and Infrastructure Engineering,* Vol. 38(17), 2472–2490. https://doi.org/10.1111/mice.13070.

[4] Tonghua, L., He, W., Zhang, S., Liu, X., Huang, F. and Liu, W., (2022). A New Method for Measuring the Relative Dielectric Constant of Porous Mixed Media using GPR, and its Application. *Construction and Building Materials,* Vol. 353. https://doi.org/10.1016/j.conbuildmat.2022.129042.

[5] Rasol, M., Pérez-Gracia, V., Assunção, S. S., González-Drigo, R., Clapes, J., Sossa, V. A. and Schmidt, F., (2022). Background Clutter Amplitude and Frequency of GPR Signals to Analyse Water Content in Sedimentary Deposits: Urban Infrastructure Environment. *Environmental Research,* Vol. 212. https://doi.org/10.1016/j.envres.2022.113189.

[6] Ling, Z., Xu, Y., Chen, R., Wong, H. K., Lai, J., Meng, X. and Liu, C., (2022). Calculation of Dielectric Constant, Loss Property and Scattering Characteristics from the Future Martian GPR Data. *Icarus,* Vol. 386. https://doi.org/10.1016/j.icarus.2022.115181.

[7] Gamal, M., Di, Q., Zhang, J., Fu, C., Ebrahim, S. and El-Raouf, A. A., (2023). Utilizing Ground-Penetrating Radar for Water Leak Detection and Pipe Material Characterization in Environmental Studies: A Case Study. *Remote Sensing,* Vol. 15(20). https://doi.org/10.3390/rs15204924.

[8] Hassan, A., Razali, M., Sulaiman, S., Idris, A., Ghazali, M., Hashim, M., and Junoh, S. (2023). Accuracy Assessment of GPR Data for Buried Objects with Different Pipes and Soil-Based Conditions. *International Journal of Geoinformatics*, Vol. 19(5), 9–18. https://doi.org/10.52939/ijg.v19i5.2651.

[9] Nicoleta, I., Savin, A., Steigmann, R. and Dobrescu, G. S., (2021). Underground Pipeline Identification into a Non-Destructive Case Study Based on Ground-Penetrating Radar Imaging. *Remote Sensing,* Vol. 13(17). https://doi.org/10.3390/rs13173494.

[10] Jin, Y. and Duan, Y., (2020). Wavelet Scattering Network-Based Machine Learning for Ground Penetrating Radar Imaging: Application in Pipeline Identification. *Remote Sensing,* Vol. 12(21). https://doi.org/10.3390/rs12213655.

[11] Chun, P. J., Suzuki, M. and Kato, Y., (2023). Iterative Application of Generative Adversarial Networks for Improved Buried Pipe Detection from Images Obtained by Ground-Penetrating Radar. *Computer-Aided Civil and Infrastructure Engineering,* Vol. 38(17), 2472–2490. https://doi.org/10.1111/mice.13070.

[12] Tesic, K., Baricevic, A., Serdar, M. and Gucunski, N., (2024). Electromagnetic Property Selection for GPR Modelling in Corrosive Concrete Environments. *Developments in the Built Environment*, Vol. 17. https://doi.org/10.1016/j.dibe.2023.100302.

[13] Zardasti, L., Yahaya, N., Noor, N. M. and Valipour, A., (2020). Quantifying Reputation Loss of Pipeline Operator from Various Stakeholders' Perspectives – Part 1: Prioritization. *Journal of Loss Prevention in the Process Industries,* Vol. 63. https://doi.org/10.1016/j.jlp.2019.104034.

[14] Halim, N., Abdullah, N., Ghazali, M., and Hassan, H. (2023). The Possibility of Using Terrestrial-Based Ground Penetrating Radar (GPR) Technology for Supplying 3rd Dimension Information for A Search and Recovery Mission for Landslide Victims. *International Journal of Geoinformatics*, Vol. 19(5), 105–118. https://doi.org/10.52939/ijg.v19i5.2669.

[15] Faris, N., Zayed, T., Abdelkader, E. M. and Fares, A., (2023). Corrosion Assessment Using Ground Penetrating Radar in Reinforced Concrete Structures: Influential Factors and Analysis Methods. *Automation in Construction,* Vol. 156. https://doi.org/10.1016/j.autcon.2023.105130.

[16] Oudart, N., Ciarletti, V., Le Gall, A., Hervé, Y. and Brighi, E., (2022). Retrieval of the Ground Dielectric Permittivity by Planetary GPR Accommodated on a Rover: Application to the Estimation of the Reflectors' Depth by the WISDOM/ExoMars Radar. *Planetary and Space Science,* Vol. 224. https://doi.org/10.1016/j.pss.2022.105606.

[17] Wong, P. T. W., Lai, W. W. L. and Poon, C. S., (2023). Classification of Concrete Corrosion States by GPR with Machine Learning. *Construction and Building Materials,* Vol. 402. https://doi.org/10.1016/j.conbuildmat.2023.132855.

[18] Li, K., Xie, X., Huang, C., Zhou, B., Duan, W., Lin, H. and Wang, C., (2023). Study on the Penetration Capability of GPR for the Steel-Fibre Reinforced Concrete (SFRC) Segment Based on Numerical Simulations and Model Test. *Construction and Building Materials*, Vol. 400. https://doi.org/10.1016/j.conbuildmat.2023.132719.